iScience

CellPress
OPEN ACCESS

Article

Hydrothermal regulation of MnO_2 on a wood-based RGO composite for achieving wide voltage windows and high energy density supercapacitors

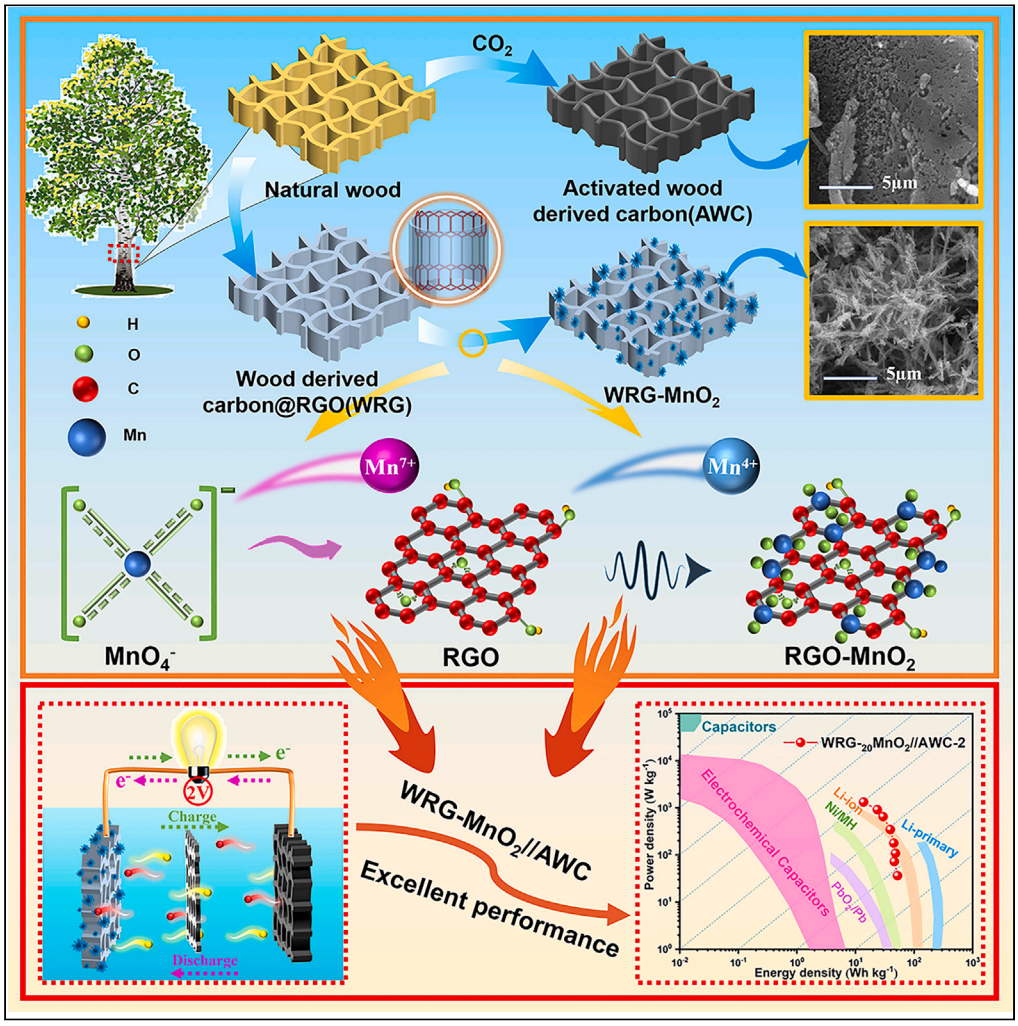

Xiaofei Shan, Li Wang, Lili Li, ..., Zhe Wang, Xiaotao Zhang, Ximing Wang

jeromew@126.com (Z.W.)
lianzixiaotao@163.com (X.Z.)
wangximing@imau.edu.cn (X.W.)

Highlights

The concept of biomass electrodes based on wood, RGO, and MnO_2 is firstly proposed

The icicle-shaped MnO_2 of WRG-MnO_2 accelerates electrons migration and ions diffusion

The packaged WRG-MnO_2/AWC shows excellent overall device performance

Shan et al., iScience 27, 109228
March 15, 2024
https://doi.org/10.1016/j.isci.2024.109228

iScience

CellPress
OPEN ACCESS

Article

Hydrothermal regulation of MnO_2 on a wood-based RGO composite for achieving wide voltage windows and high energy density supercapacitors

Xiaofei Shan,[1] Li Wang,[2] Lili Li,[1] Ya Zuo,[3] Zhenghua Fu,[4] Jing Wu,[1] Zhe Wang,[1,*] Xiaotao Zhang,[3,*] and Ximing Wang[1,5,*]

SUMMARY

The increasing need for improved energy storage devices renders it particularly important that inexpensive electrodes with high capacitance, excellent cycling stability, and environment-friendly characteristics are developed. In this study, a wood-derived carbon@reduced graphene (WRG) conductive precursor with an average conductivity of 15.38 S/m was firstly synthesized. The binder-free WRG-MnO_2 electrode was successfully constructed by growing MnO_2 onto a WRG under hydrothermal conditions. The asymmetric supercapacitor assembled with the WRG-$_{20}MnO_2$ cathode exhibited excellent electrochemical capacitive behavior with a voltage window of 0–2 V, maximum energy density of 52.3 Wh kg^{-1}, and maximum power density of 1642.7 W kg^{-1}, which is mainly due to the distinctive icicle-shaped structure of the MnO_2. Thus, a facile strategy for developing high-performance hierarchical porous carbon electrodes that can be used in supercapacitors was developed herein, which may provide new opportunities to improve the high added value of poplar wood.

INTRODUCTION

The critical shortage of fossil resources and increasingly severe environmental pollution renders the development of sustainable and low-cost energy storage devices increasingly urgent.[1] Supercapacitors (SCs), with advantages such as fast charging and discharging, a long lifespan, and high power density, are therefore particularly attractive green energy storage devices for use in fields such as solar-power generation, wind-power generation, and hybrid vehicles.[2,3] However, the low energy density of SCs limits their application in automobiles and consumer electronics.[4,5] Increasing the voltage window is one effective means of improving the energy density of SCs. The storage energy capability of electrochemical energy storage devices, such as SCs and lithium-ion batteries, also strongly relies on the properties of the electrode material, including its micromorphology, conductivity, and specific surface area.).[6–9] The good electrical conductivity and high chemical stability of carbon-based electrode materials, such as graphene or porous carbon, render them promising candidates for SCs,[10] and recent advances have led to the development of numerous new electrode materials, such as carbon materials,[11,12] metal oxides,[13–15] and conductive polymers,[16–18] that can further improve the performance of SCs. These electrode materials are typically in powder form and thus binders and conductive additives are required to obtain precursor ink, which is then coated onto current collectors as substrates, increasing the weight of the obtained electrode without increasing the energy density. However, the coating process can result in inferior electrode structures that limit fast electronic and ionic conduction.[19] In this context, the primary challenge of electrode design is achieving a wide voltage window while maintaining low tortuosity, deformability, and high ionic and electronic conductivity.[20]

Wood has a unique three-dimensional (3D) hierarchical porous structure that comprises large numbers of vertical vessels (30–130 μm) running along the growth direction of the tree, through which ions, water, and other nutrients are transported around the tree.[21,22] This porous structure mainly comprises tracheids, vessels, and cellulose fibers comprising different arrangements of lignin and hemicellulose and is particularly conducive to the rapid transport of ions and electrons.[23] The natural mechanical structure that is formed by cellulose, hemicellulose, and lignin is similar to reinforced concrete, rendering it a natural precursor for independent carbon electrodes;[24] the 3D hierarchical network increases the interaction between electrolyte and electrode surface while also offering a large surface area for the deposition of active materials.[25–29] Therefore, several researchers have investigated the use of conductive carbonized wood as an electrode material for SCs. However, as a type of carbonaceous material, the limited energy storage capacity that is associated with carbonized wood hinders its energy density,[30] and the oxygen-sensitive functional groups on the surface of carbonized wood are highly active and reduce the energy storage performance

[1]School of Materials Science and Art Design, Inner Mongolia Agricultural University, Saihan District, Hohhot City, Inner Mongolia Autonomous Region 010010, China
[2]Inner Mongolia University of Science and Technology, Kundulun District, Baotou City, Inner Mongolia Autonomous Region 014017, China
[3]College of Science, Inner Mongolia Agricultural University, Saihan District, Hohhot City, Inner Mongolia Autonomous Region 010010, China
[4]Lufumei Furniture Co., Ltd, Baotou City, Inner Mongolia Autonomous Region 014017, China
[5]Lead contact
*Correspondence: jeromew@126.com (Z.W.), lianzixiaotao@163.com (X.Z.), wangximing@imau.edu.cn (X.W.)
https://doi.org/10.1016/j.isci.2024.109228

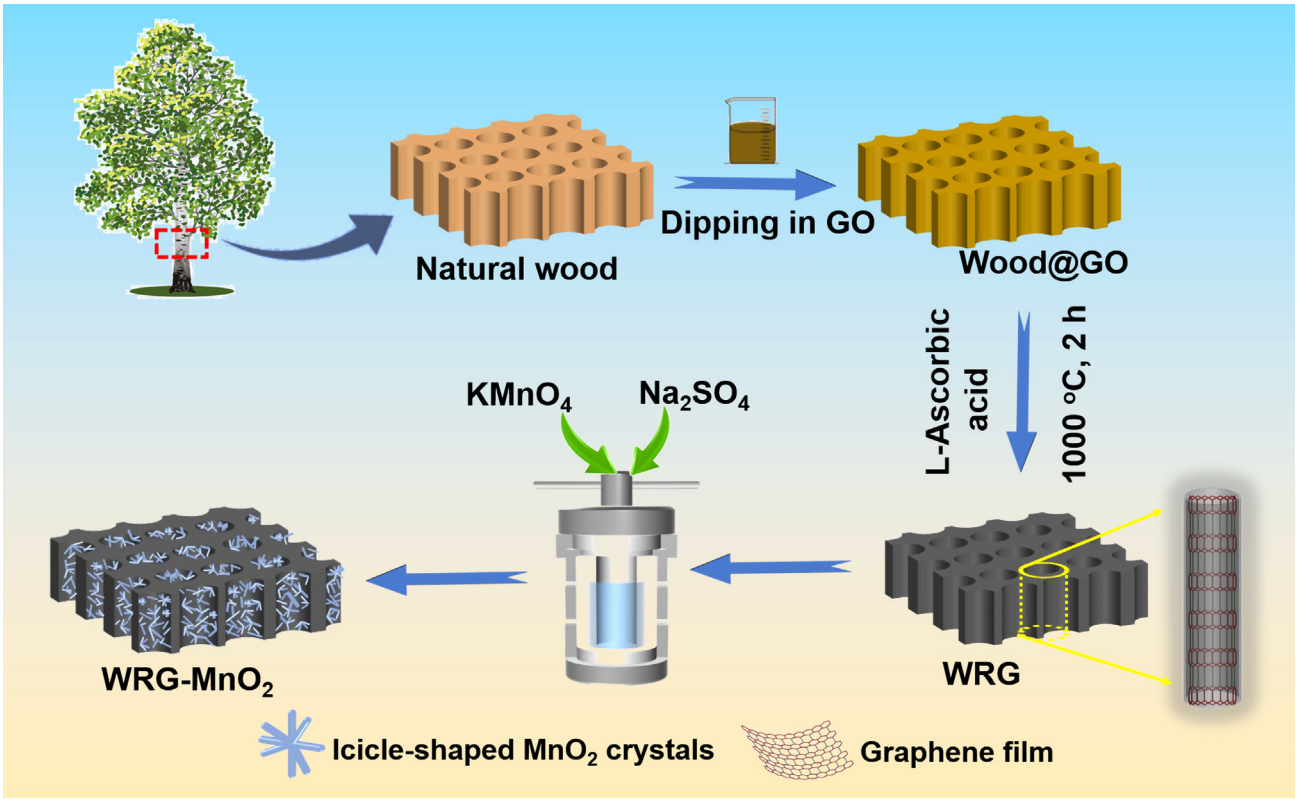

Scheme 1. Schematic illustration showing the preparation process of the WRG-MnO_2 electrode

and cyclic stability of a produced SC.[20,31] Thus, the power and energy density of wooden energy storage devices are often improved by introducing other components, such as metal oxides, polymers, and heteroatoms.[20,32,33]

MnO_2 is a typical electrode pseudocapacitor that has characteristics such as high specific capacitance (theoretically reaching up to 1370 F g^{-1} based on a one-electron redox reaction per manganese atom),[34] low cost, and satisfactory environmental compatibility. However, the poor electronic conductivity of MnO_2 (~10^{-8} S cm^{-1}) hinders its practical application in energy devices.[35] To address the intrinsic limitations and maximize the utilization of MnO_2 as a pseudocapacitor, one common strategy is to integrate low-dimensional oxide materials such as MnO_2 with highly conductive substrates, such as carbon materials.[36–38] Wan et al. prepared a free-standing and binder-free SC electrode by compounding wood biochar with MnO_2,[32] with results showing a moderate specific capacitance of 101 F g^{-1} at a current density of 0.05 A g^{-1}, excellent Coulombic efficiency of 98%–100%, and favorable cyclic stability with a capacitance retention of 85.0% after 10,000 cycles. Further, carbon materials, such as carbon nanotubes (CNTs),[39,40] graphene,[41–43] and porous carbon,[44–46] exhibit better cycling stability, higher rate capabilities, and wider working voltages than pseudocapacitive materials. Graphene sheets are promising carbon materials for use as SCs owing to their high specific surface area, superior conductivity, and stable lattice structure.[47–50] However, the stacking effect of graphene hinders the transport of ions and the infiltration of electrolytes into the electrode material, reducing its actual specific capacity. Wu et al. fabricated a wood-derived, porous ACW@RGO electrode by infiltrating graphene oxide (GO) into the directional pores of wood,[51] with the resulting electrode exhibiting an outstanding areal specific capacitance of 26.6 F cm^{-2} at a current density of 1 mA cm^{-2}.

In line with previous research, this study aimed at successfully synthesizing a wood-derived carbon@RGO-MnO_2 (WRG-MnO_2) electrode using a simple hydrothermal method. RGO was uniformly distributed within the 3D pores structure of carbonized wood as continuous layers, forming interconnected conductive network structures upon which MnO_2 could grow evenly. The unique icicle-shaped MnO_2 crystal structure was found to greatly accelerate the transport of ions. The electrochemical performance of the newly constructed WRG-MnO_2 electrode was characterized using capacitance as a measurement indicator. An asymmetric supercapacitor (ASC) was constructed with activated wood-derived carbon (AWC) as the anode material, and its overall performance was further analyzed under the two-electrode system.

RESULTS

The overall synthesis process of the WRG-MnO_2 electrode is shown in Scheme 1. First, wood was processed into thin pieces and GO solution was infiltrated into the pores of the wood using the vacuum impregnation method. Conductive graphene was then grown onto the wood via a combination of ascorbic acid reduction and thermal reduction. The resulting self-standing WRG-MnO_2 electrode formed without the use of any adhesive and conductive agent was successfully prepared using the simple hydrothermal method. The electrode exhibited the following

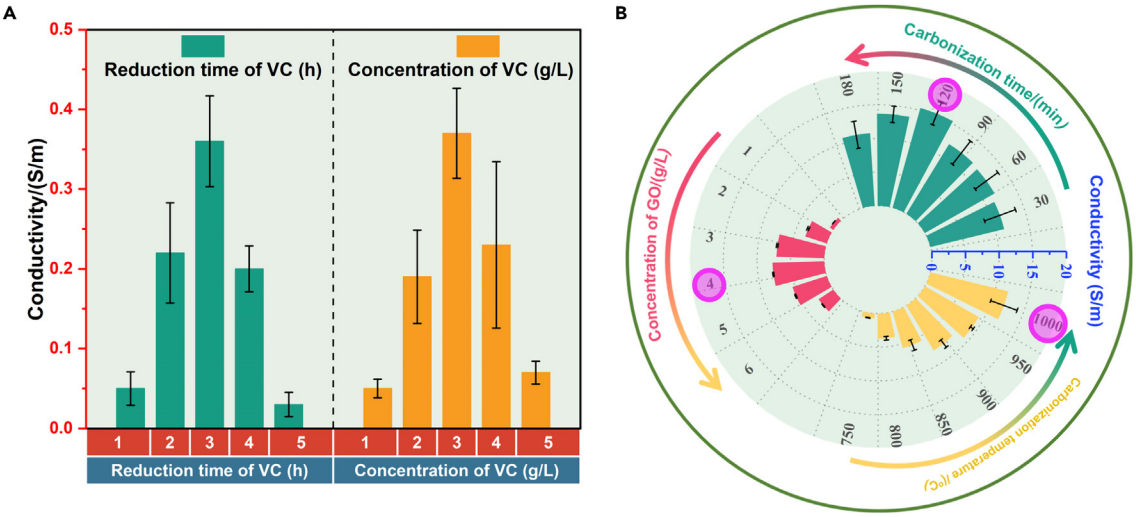

Figure 1. Conductivity of the WRG precursor

(A) Conductivity changes under VC reduction conditions.

(B) Conductivity changes under carbonization conditions.

unique advantages: (1) The WRG conductive precursor retained the 3D multilevel straight-through channel network structure of the wood, which is an ideal collector material for pooling currents. (2) The excellent conductivity of RGO was conducive to improving the rate performance of the electrode. (3) The unique icicle-shaped MnO_2 crystals that were synthesized through hydrothermal regulation greatly improved the specific capacitance of the electrode.

Analysis of WRG conductivity

The conductivities of the WRG precursors were studied to prove that the WRG can be used as a self-standing conductive fluid collector. The carbon content of GO increased to ~90% following high-temperature thermal deoxidation; however, the conductivity remained low because of the residual defects on the graphene sheet. Chemical reduction in the form of treating wood@GO with ascorbic acid (3 g/L) over 3 h was therefore performed to improve the electrical conductivity of the obtained WRG. As shown in Figure 1A, the conductivity of the WRG precursors increased from 0 S/m for wood@GO to 0.37 S/m for WRG treated with ascorbic acid at a concentration of 0–5 g/L. This result indicates that GO was reduced and that the defects on the graphene sheet were removed to a certain extent. On this basis, defect removal was further performed through high-temperature heat treatment. The WRG precursor demonstrated the best conductivity (15.38 S/m) using 4 g/L of the GO solution during carbonization (2 h, 1,000°C), which is ~40% higher than that of the WRG precursor obtained via ascorbic acid reduction (Figure 1B). This reveals that heat treatment further improves the final improvement effect of the graphene structure.

Characterization of WRG-MnO_2 as the cathode material

The morphologies and structures of different materials were characterized via SEM and TEM. Abundant 3D hierarchical pore structures (macropores, mesopores, and micropores) were observed within the wood, as seen in Figures 2A and 2B). These long, straight channels provided a natural channel structure for the uniform distribution of layered graphene. Interestingly, the WC still retained the structural advantage of graded wood porosity, facilitating the rapid transport of electrons and electrolyte ions. Uniform layers of graphene in the WC channels (Figure 2C) were in stark contrast with the icicle-shaped MnO_2 crystals that were observed in the RGO along the inner wall of the wood conduit as a result of hydrothermal regulation (Figure 2D). Importantly, as the concentration of $KMnO_4$ increased, the morphology also underwent considerable changes, with the initially-generated MnO_2 exhibiting a lamellar structure (Figures S1A–S1C); however, as the amount of MnO_2 increased, the structure of the MnO_2 changed to form small spheres with uneven surfaces (Figures S1D–S1F), followed by convex icicle shapes, which resulted from the self-assembly behavior of the clusters (Figures 2E–2G), and ultimately large spherical shapes with smooth surfaces (Figures S1G–S1I)). The icicle-shaped MnO_2 crystal structure can greatly shorten the electron transfer path, which is conducive to rapid electron transfer. An interesting phenomenon was also observed in Figure 2H, in which RGO film formed spontaneously within the wood conduit via self-assembly. Moreover, nano-MnO_2 crystals grew uniformly on the thin RGO films, indicating that the self-assembly behavior of the graphene increased the growth area of the MnO_2, which was particularly conducive to improving the specific capacitance of the electrode. This is mainly due to the oxidation–reduction reaction that occurs between carbon and $KMnO_4$ under hydrothermal conditions (Equation 1), which allows MnO_2 to grow on the graphene without shedding. TEM observation further confirmed that nano-MnO_2 crystals had grown *in situ* on the wood carbon and graphene films via the hydrothermal reaction (Figures 2I and 2J)) and that nano-MnO_2 crystals exhibited a long needle shape, which was consistent with the SEM results and further confirmed the *in situ* growth of MnO_2 on the graphene.

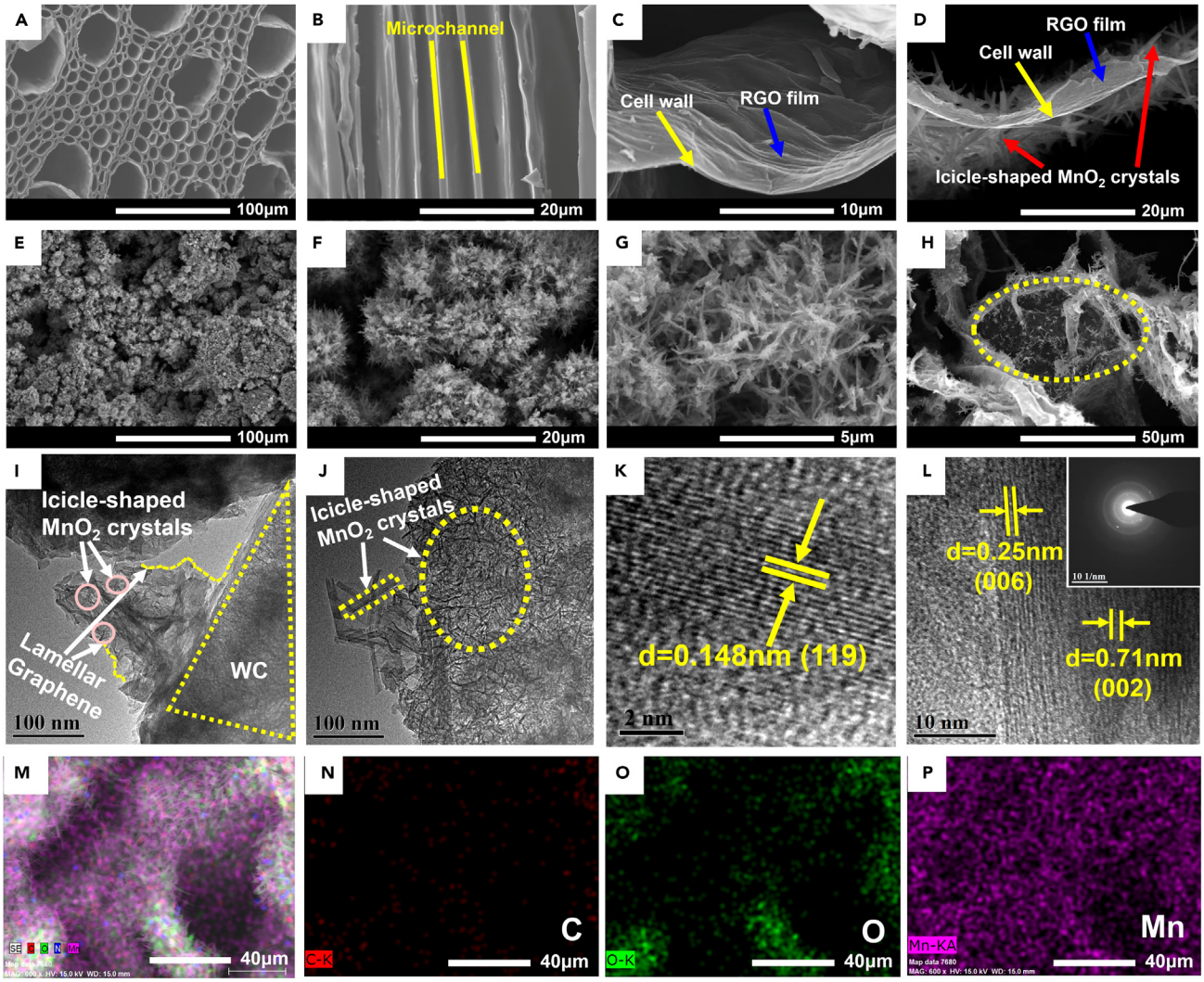

Figure 2. Microstructural characterizations of materials

(A and B) SEM images of WC: (A) Transverse section and (B) longitudinal section.

(C) Cell wall of the WRG precursor.

(D) Cell wall of the WRG-$_{20}$$MnO_2$ electrode.

(E–H) SEM images of the WRG-$_{20}$$MnO_2$ electrode at different magnifications.

(I and J) TEM images of the WRG-$_{20}$$MnO_2$ electrode.

(K and L) HR-TEM images of the WRG-$_{20}$$MnO_2$ electrode, with SAED pattern inset.

(M–P) Element mapping images of the WRG-$_{20}$$MnO_2$ electrode: (M) Total spectrum, (N) C, (O) O, (P) Mn.

The crystal structure of the WRG-$_{20}$$MnO_2$ electrode was then studied through HR-TEM. Figures 2K and 2L) show the parallel interatomic planar spacing of 7.1, 2.5, and 1.48 Å, which correspond to the typical (002), (006), and (119) crystallographic planes of the birnessite-type MnO_2 phase, respectively. The three concentric circles in the electron diffraction (SAED) results in Figure 2L indicate the polycrystalline structure. The above results indicate the successful loading of MnO_2 onto the WRG precursor, while the EDX mapping images of the WRG-$_{20}$$MnO_2$ electrode also prove that C, O, and Mn are uniformly present within the structure of the WRG-$_{20}$$MnO_2$ electrode, with both C and O covered by large amounts of Mn (Figures 2M–2P).

The crystalline structure of the samples was further studied via XRD. As shown in Figure 3A, the XRD patterns of the WC and WRG showed two wide peaks at 26° and 44°, which corresponded to the (002) and (100) diffraction planes of the graphite layer structure, respectively. The WRG-$_{20}$$MnO_2$ electrode exhibited new characteristic peaks at 12.3°, 36.8°, and 65.7°, corresponding to the (002), (006), and (119) diffraction peaks of the birnessite-type MnO_2 (JCPDS no. 18–0802) crystal phase, respectively. In general, birnessite-type MnO_2 nanostructures can be coated *in situ* onto the outer surface of various carbon materials by redox deposition, creating an intimate connection with the conducting carbons.[52,53] Raman spectroscopy was used to evaluate the defect degree of the electrode, as seen in Figure 3B, with WC, WRG, and

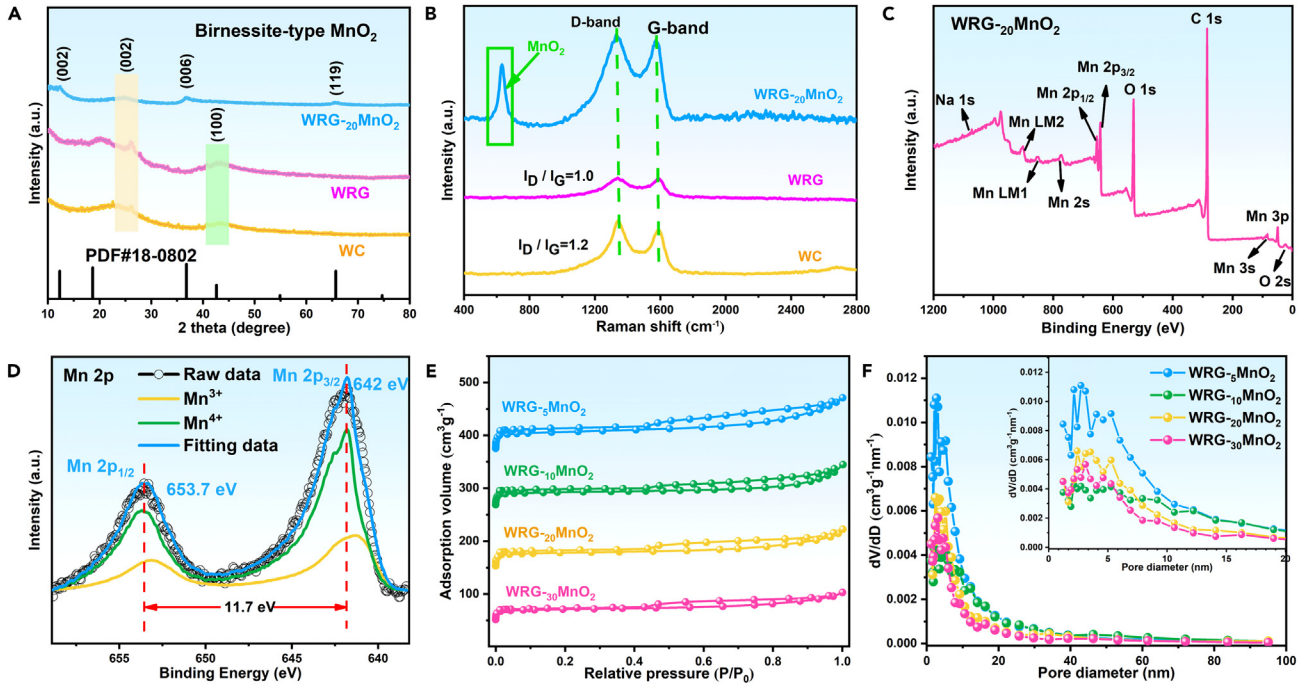

Figure 3. Chemical analysis of materials

(A) XRD patterns of WC, WRG, and WRG-$_{20}$MnO$_2$.

(B) Raman patterns of WC, WRG, and WRG-$_{20}$MnO$_2$.

(C and D) XPS spectra of the WRG-$_{20}$MnO$_2$ electrode: (C) Survey XPS and (D) high-resolution Mn 2p spectra.

(E) N_2 adsorption–desorption isotherms of WRG-MnO$_2$.

(F) Pore diameter distribution of WRG-$_{20}$MnO$_2$.

WRG-$_{20}$MnO$_2$ exhibiting characteristic peaks indicating atomic carbon crystals; the D peak at 1340 cm^{-1} indicated a defect in the C atom lattice, while the G peak at 1580 cm^{-1} represented an in-plane stretching vibration of the C atom sp^2 hybrid. The intensity ratio of the D to G peak (I_D/I_G) represented the degree of disorder in the carbon materials.[54] Introducing the RGO led to a decrease in the ratio of I_D/I_G from 1.2 to 1.0, indicating a decline in the disordered structure of the material. The Raman bands obtained for MnO$_2$ were attributed to the Mn–O stretching vibration in the [MnO$_6$] octahedra (501 cm^{-1}), Mn–O stretching in the basal plane of the [MnO$_6$] sheets (575 cm^{-1}), and symmetric Mn–O stretching of the [MnO$_6$] group (645 cm^{-1}).[55] A strong characteristic peak indicating MnO$_2$ at 645 cm^{-1} in the WRG-$_{20}$MnO$_2$ spectrum indicated that the MnO$_2$ was successfully synthesized in the WRG-$_{20}$MnO$_2$ electrode. XPS was then used to further verify the chemical state of the Mn in the WRG-$_{20}$MnO$_2$ electrode. The survey spectrum in Figure 3C indicated that the WRG-$_{20}$MnO$_2$ electrode contained C, O, and Mn. Figure 3D shows the high–resolution XPS spectra of Mn 2p, the spectra was distributed into two different peaks (Mn^{3+} and Mn^{4+}) at the binding energy of 653 and 653.3eV for Mn 2p$_{1/2}$ and 641.3, 641.8eV for Mn 2p$_{3/2}$, respectively. In addition, to evaluate the contribution of Mn^{3+} and Mn^{4+}, the ratio of peak area was used to determine the relative proportion of Mn^{3+} and Mn^{4+}. The results show that the molar ratio of Mn^{3+} and Mn^{4+} was 2:5, and the spin–orbit coupling separation energy of Mn 2p$_{1/2}$ (653.7eV) and Mn 2p$_{3/2}$ (642 eV) was 11.7 eV, proving that the oxidation state of Mn in the WRG–$_{20}$MnO$_2$ electrode material is Mn^{4+} (MnO$_2$).[56]

Furthermore, the N_2 adsorption–desorption curves of the WRG-MnO$_2$ electrode further reflected the changes in the specific surface area and pore size distribution after MnO$_2$ loading. As shown in Figure 3E, according to the IUPAC classification,[57] the nitrogen adsorption/desorption isotherm of the WRG-MnO$_2$ electrode was a typical IV type, indicating a mesoporous structure. It is worth noting that the WRG-$_{20}$MnO$_2$ electrode had the largest specific surface area of 98.93 m^2 g^{-1} (Table S1). The WRG-$_{20}$MnO$_2$ electrode has a large specific surface area as well as is a mesoporous material that allows the easy diffusion of electrolyte ions, which pass through the electrode and electrolyte interface.[58] In addition, the pore size distribution of the WRG-MnO$_2$ electrode material was estimated using BJH analysis, with the results in Figure 3F also demonstrating mesoporous (2–50 nm) characteristics and an average pore diameter of 5.9 nm for the WRG-MnO$_2$ electrode (Table S1). The high specific surface area, active reaction sites, and higher transport efficiency of the reactants in the mesoporous structure render the electrode more conducive to energy conversion and storage.[59]

To further enhance the charge storage capacity of the wood-based thick electrodes, the entire electrode thickness was designed to be 570 μm (Figure 4A). The amount of MnO$_2$ loaded was controlled by the concentration of KMnO$_4$ under the specific reaction equation (Equation 1)). As seen in Figure 4B, the amount of MnO$_2$ loaded increased with the addition of KMnO$_4$, with 7.14, 13.19, 27.38, and 40.26 mg cm^{-2} observed for the WRG-$_5$MnO$_2$, WRG-$_{10}$MnO$_2$, WRG-$_{20}$MnO$_2$, and WRG-$_{30}$MnO$_2$ electrodes, respectively. CV was conducted on the

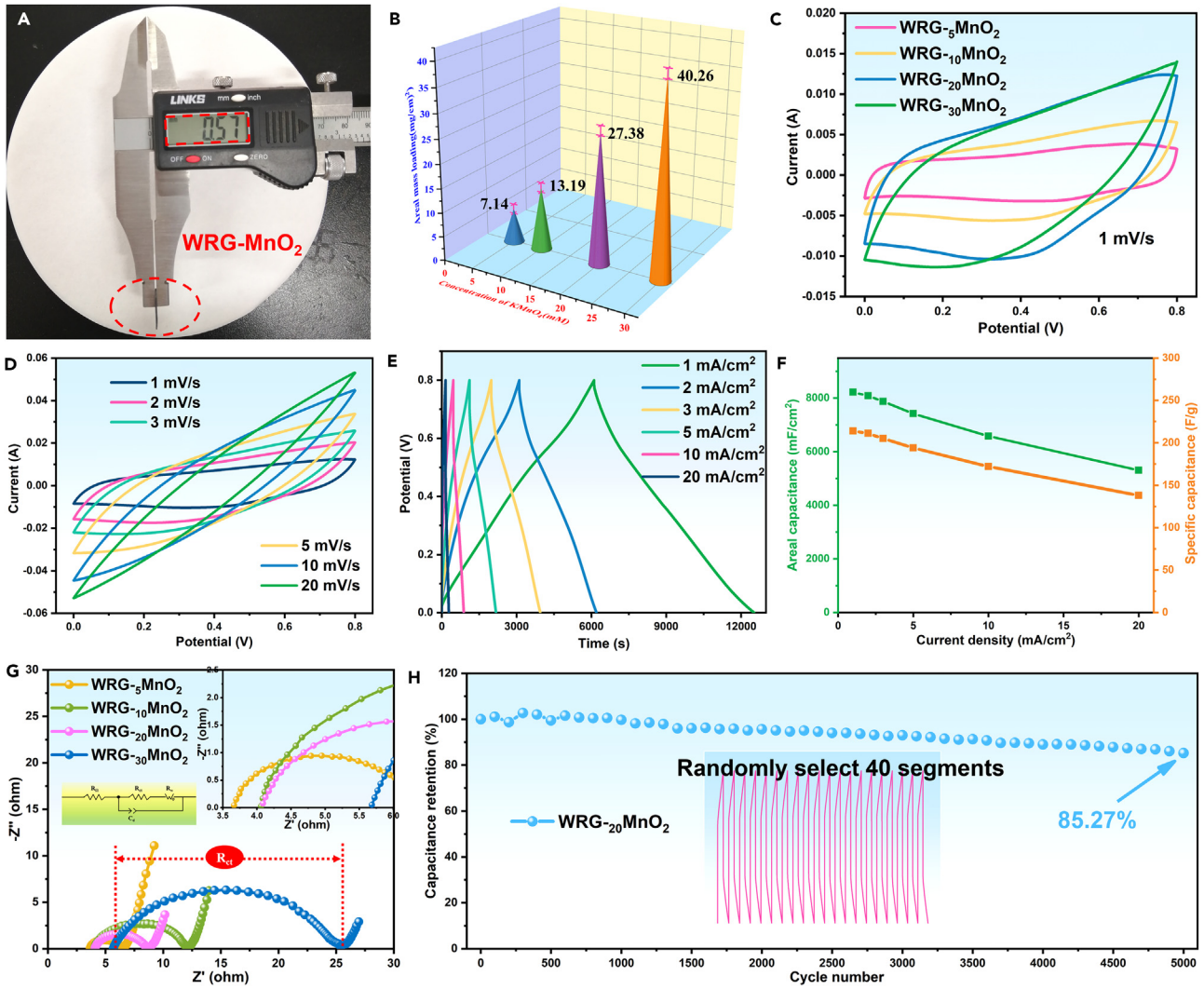

Figure 4. Electrochemical characterizations of WRG-MnO_2 electrodes

(A) Thickness measurement of the WRG-MnO_2 electrode.

(B) Different $KMnO_4$ concentrations correspond to the areal mass loading of MnO_2 in the WRG-MnO_2 electrode.

(C) CV curves of the WRG-MnO_2 electrode at 1 mV s^{-1}.

(D–F) Electrochemical performance of the WRG-$_{20}MnO_2$ electrode: (D) CV curves obtained at different scan rates. (E) GCD curves obtained at different current densities. (F) Rate performance.

(G) Nyquist diagram of the WRG-$_5MnO_2$, WRG-$_{10}MnO_2$, WRG-$_{20}MnO_2$, and WRG-$_{30}MnO_2$ electrodes (illustrated as a partially enlarged Nyquist diagram).

(H) Cycling performance of the WRG-$_{20}MnO_2$.

electrodes in the three-electrode system for a more effective evaluation of the electrochemical performance of the WRG-MnO_2 electrodes. Figure 4C shows the CV curve at a scan rate of 1 mV s^{-1} and potential range of 0–0.8 V. It is apparent from the figure that the area enclosed by the CV curves gradually rises as the MnO_2 loading increases. This result directly proves that the MnO_2 content affects the charge storage capacity of the electrode. Of the electrodes tested, the closed area of the WRG-$_{20}MnO_2$ electrode was obviously improved as compared to the other electrodes.

$$4MnO_4^- + 3C + H_2O \rightarrow 4MnO_2 + CO_3^{2-} + 2HCO_3^-. \quad \text{(Equation 1)}$$

The electrochemical performance of the prepared electrode was further evaluated in the three-electrode system. As seen in Figure 4D, the WRG-$_{20}MnO_2$ electrode demonstrated near-mirror symmetry characteristics and there was no obvious redox peak, reflecting typical double-layer capacitance characteristics. In addition, the WRG-$_{20}MnO_2$ electrode had the largest curve closure area compared to the other electrodes (WRG-$_5MnO_2$, WRG-$_{10}MnO_2$, and WRG-$_{30}MnO_2$) (Figures S2A, S2D, and S2G). The GCD curves of all the electrodes were in the shape

of an isosceles triangle, which was explained by the ideal double-layer capacitance behavior of the electrode and is consistent with the CV curves of the electrodes (Figures 4E, S2B, S2E, and S2H)). In Figures 4F, S2C, S2F, and S2I), the WRG-$_{20}$MnO$_2$ electrode shows excellent rate performance with an areal capacitance (specific capacitance) of 8.22 F cm^{-2} (214 F g^{-1}) at 1 mA cm^{-2}, with the areal capacitance of the WRG-$_5$MnO$_2$, WRG-$_{10}$MnO$_2$, and WRG-$_{30}$MnO$_2$ electrodes at 2.36, 4.02, and 11.9 F cm^{-2}, respectively. The areal capacitance of the electrode grows continuously as the MnO$_2$ loading increases; however, it is worth noting that the voltage drop in the GCD discharge curve of the WRG-$_{30}$MnO$_2$ electrode is considerably higher than that of any other electrode (at a current density of 1 mA cm^{-2}, the voltage drop of WRG-$_{30}$MnO$_2$ is 0.0501V, WRG-$_5$MnO$_2$ is 0.0145V, WRG-$_{10}$MnO$_2$ is 0.0291V, and WRG-$_{20}$MnO$_2$ is 0.0191V), which may be the result of excessive MnO$_2$. The agglomeration effect caused by excessive MnO$_2$ directly hinders the transfer of electrons and ions, increasing the resistance and reducing the conductivity of the electrode. Moreover, the unique icicle-shaped crystal structure of the MnO$_2$ accelerates the rapid transfer of the electrons, improving the electrochemical performance of the electrode. Compared with similar carbon-based MnO$_2$ electrodes, the WRG-$_{20}$MnO$_2$ electrodes also exhibited outstanding rate performance (Table S2).

Electrochemical impedance was used to evaluate the electronic conductivity and charge transport characteristics of the electrodes in the frequency range of 10^5–10^{-2} Hz at an internal alternating current (AC) disturbance of 5 mV. Figure 4G shows the Nyquist diagrams of the WRG-$_5$MnO$_2$, WRG-$_{10}$MnO$_2$, WRG-$_{20}$MnO$_2$, and WRG-$_{30}$MnO$_2$ electrodes, with the corresponding equivalent fitting circuit diagram. The Nyquist diagram is semicircular in the high-frequency region and linear in the low-frequency region. In addition to the double-layer capacitance formation (C_{dl}), the first intercept at high frequency between the semicircle and the transverse axis represents the internal bulk resistance (R_Ω), which includes the ionic resistance of the electrolyte solution and the intrinsic resistance of the active material,[60] while the diameter of the semicircle reflects the charge transfer resistance (R_{ct})[61] and the linear part reflects the Warburg impedance (Z_w), which is caused by the diffusion of electrolytic ions onto the surface electrode. The x-intercept of the high-frequency part of the Nyquist plot shows that the conductivity of the WRG-$_5$MnO$_2$, WRG-$_{10}$MnO$_2$, WRG-$_{20}$MnO$_2$, and WRG-$_{30}$MnO$_2$ electrodes is gradually worsening. This occurs because as the loading increases, nano-MnO$_2$ gradually agglomerates, making its conductivity poor. The excess MnO$_2$ inhibits the WRG precursor, limiting the conductivity of the WRG precursor, increasing the R_Ω of the electrode, and decreasing the conductivity of the electrode. The WRG-$_{20}$MnO$_2$ electrode has the lowest R_{ct} (4.5 Ω) as compared to WRG-$_{10}$MnO$_2$ (8.1 Ω) and WRG-$_{30}$MnO$_2$ (19.7 Ω), indicating that WRG-$_{20}$MnO$_2$ has considerable advantage for the charge transport capability. In the mid frequency region, the projection length of the Warburg impedance curve on the Z′ axis characterizes the ion penetration process. Obviously, the Warburg length of the WRG-$_{20}$MnO$_2$ electrode is shorter than that of other electrodes (WRG-$_5$MnO$_2$, WRG-$_{10}$MnO$_2$ and WRG-$_{30}$MnO$_2$), which indicates that the WRG-$_{20}$MnO$_2$ electrode has the shortest ion diffusion path. This is mainly attributed to the icicle shapes nano MnO$_2$ structure. In addition, the cycling performance of WRG-$_{20}$MnO$_2$ was investigated (Figure 4H), with results showing that 85.3% of its initial capacitance was retained after charging and discharging for 5,000 cycles at 10 mA cm^{-2}, demonstrating its excellent cycling performance. The GCD curve maintained almost the same shape in 20 randomly selected cycles (illustrations for Figure 4H), demonstrating the outstanding reversibility of the WRG-$_{20}$MnO$_2$ electrode. The above results demonstrate that the WRG-$_{20}$MnO$_2$ electrode has excellent electronic conductivity and charge transfer characteristics, indicating its obvious advantages in the use of SCs with high energy density.

Conductivity and energy storage mechanism of the WRG-MnO$_2$ cathode material

The conductive and energy storage mechanisms of the WRG-$_{20}$MnO$_2$ electrode were also examined in detail to gain a more comprehensive understanding of its working performance. The results indicated that the –OH and –COOH in the GO were chemically bonded to the –OH in the wood to form hydrogen bonds as a result of vacuum impregnation, anchoring GO tightly to the wood. Figure 5 shows the conduction and energy storage mechanism of the WRG-MnO$_2$ electrode. After filling the wood with RGO, the wood surface and inner microchannel wall were observed to be fully covered by lamellar RGO. Several oxygen-containing groups from wood@GO (–COOH, –OH, C=O, –C–O–C) were removed in the form of H$_2$O and CO$_2$ during thermal reduction. The thermal decomposition of the oxygen-containing groups reduced the binding of oxygen atoms to the electrons on the carbon atoms, thereby promoting the rapid migration of electrons onto the carbon plane in the interconnected microchannel structure. The RGO obtained by the reduction endowed the WRG precursor with high conductivity characteristics, and the lamellar graphene provided a large specific surface area for the loading of nano-MnO$_2$. When WRG and KMnO$_4$ underwent hydrothermal reaction, the C–Mn bond that formed to produce MnO$_2$ was connected via bonding, effectively improving the capacitive characteristics of the electrode.

Characterization of AWC as the anode material

The importance of the negative electrodes that are used in energy storage devices cannot be ignored. Here, we investigate the effect of activation time on the AWC performance. Analysis of the morphology structure of the AWC electrode demonstrated that increasing numbers of pores appear on the AWC electrode as the CO$_2$ activation time is prolonged (Figures 6A, 6B, and S3). However, the pores on the AWC-1 electrode are relatively sparse and unevenly distributed. The hole etching in the AWC-3 electrode is relatively serious, as manifested by the increasingly random pore structure. In comparison, the new holes that are etched in the AWC-2 electrode are uniform, with a more regular structure, and exhibit improved microscopic morphology. The CV and GCD curves also demonstrate that AWC-2 has better capacitive performance (Figures 6C and 6D). Figure 6E shows a typical CV curve obtained at a scan rate of 1–20 mV s^{-1} over a scan window of −1.2–0.8 V. The CV curve shows a nearly rectangular shape even at a high scan rate of 20 mV s^{-1}. Compared with the CV curves for AWC-1 and AWC-3, the CV curve of AWC-2 also exhibits the largest closed pattern area (Figures S4A and S4D), indicating that the AWC-2 electrode has excellent specific capacitance. The GCD curves show a nearly triangular shape for all AWC electrodes at 1–20 mA cm^{-2} (Figures 6F, S4B, and S4E). Surprisingly,

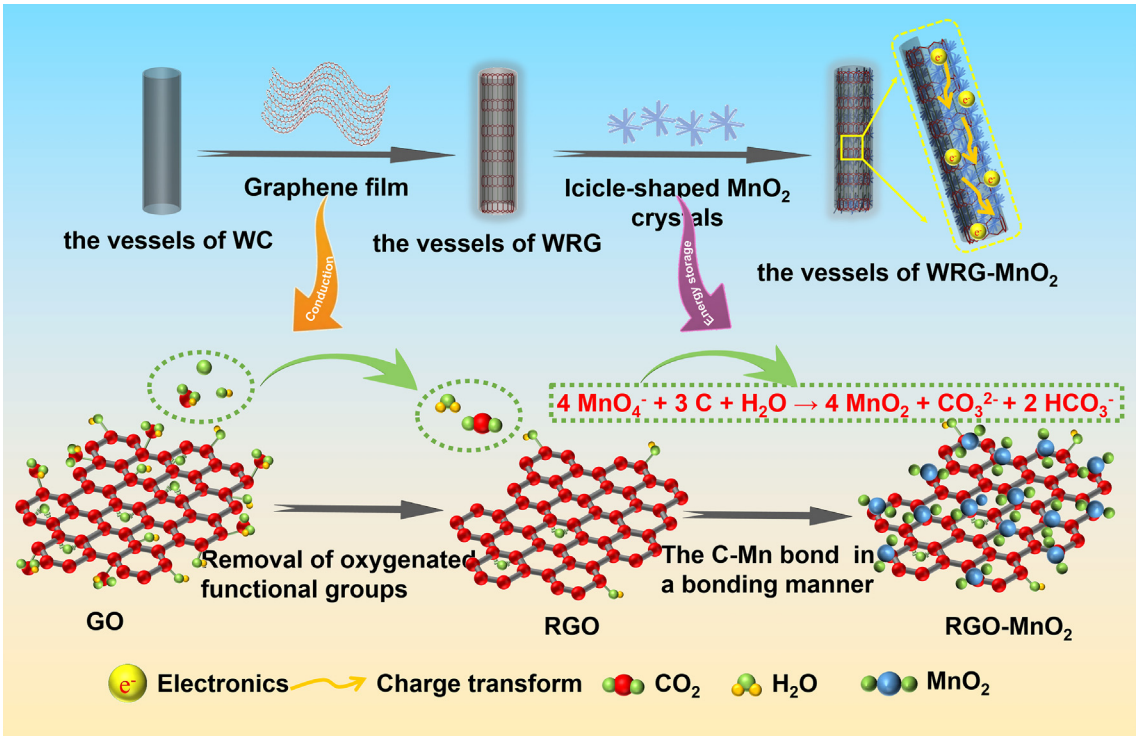

Figure 5. Diagram showing the conductivity and energy storage mechanism of the WRG-$_{20}$MnO$_2$ electrode

the AWC-2 electrode shows excellent capacitance performance, with corresponding areal capacitances of 5.8, 4.54, 4.08, 3.58, and 3.13 F cm^{-2} at current densities of 1, 2, 3, 5, and 10 mA cm^{-2}, respectively; moreover, even at an ultrahigh current density of 20 mA cm^{-2}, the AWC-2 still retains an areal capacitance of 2.76 F cm^{-2} (Figure 6G). Compared with the other electrodes (AWC-1 and AWC-3), the AWC-2 electrode also holds the highest areal capacitances (Figures S4C and S4F). The above excellent electrochemical performance obtained for the AWC-2 electrode can be attributed to the following reasons: 1) the AWC-2 electrode has a graded porous structure, which promotes the efficient penetration of electrolytes inside the electrode; 2) the AWC-2 electrode shows low curvature throughout the channel, enabling fast ion transport; 3) the conductive 3D carbon network structure of the AWC-2 electrode ensures rapid electron transport. The Nyquist diagram of the AWC electrode also indicates the excellent electronic conductivity and charge transport characteristics obtained for the AWC-2 electrode (Figure 6H), which is consistent with the above analysis. Figure 6I shows that the GCD curve of AWC-2 remains almost unchanged after 20 charge and discharge cycles.

Electrochemical performances of the WRG-$_{20}$MnO$_2$//AWC-2

One of the characteristics of ASCs is their high energy and power density. The operating voltage window of the ASC can be widened using different combinations of cathodes and anodes at opposite potential windows, rendering the electrode promising for practical application. The WRG-$_{20}$MnO$_2$//AWC-2 ASC was constructed using an AWC electrode as the anode, a cellulose membrane as the diaphragm, and a WRG-$_{20}$MnO$_2$ electrode as the cathode. The ASC was assembled and measured in a 1-M Na_2SO_4 electrolyte. The ASC model diagram and electron migration path are exhibited in Figure 7A. The natural porous structure of wood provides sufficient exchange space for the migration of electrons and ions. A voltage window of 0–2 V was obtained for the fabricated ASC device. Figure 7B shows the CV curve of ASC at different scan rates (5–100 mV s^{-1}) within the stable voltage range of 0–2 V. Increasing the scan rate led to a gradual increase in the area enclosed by the CV curve, and the rectangular shape is retained at a scan rate of 100 mV s^{-1}, indicating that the device has ideal capacitance behavior. To better understand the energy storage behavior of ASC, the contribution of capacitance to the total stored charge was studied using the CV method. It is known that the generated current mainly comes from capacitance-controlled (i_{cap}) and diffusion-controlled (i_{diff}) processes, with the calculation relations shown in Equations 2 and 3. The b values in the equations, which range from 0.5 to 1.0, imply a "transition" area between the diffusion-controlled process and pseudocapacitive behavior.[62] It is worth noting that a b value of 0.5 indicates diffusion contribution, with smaller values indicating greater diffusion contribution, while a b value of 1.0 indicates capacitance contribution, with larger b values indicating greater capacitance contribution. From Figure 7C, it can be seen that the b values under different voltages are mainly distributed in the range of 0.5–1.0. It demonstrates that the energy storage reaction of ASC is a reaction mechanism under the dual effects of pseudocapacitive behavior and diffusion control. Furthermore, the contribution of the pseudocapacitive behavior appears to be more pronounced than the diffusion control, reflecting the storage behavior of the pseudocapacitive charges. Throughout the entire

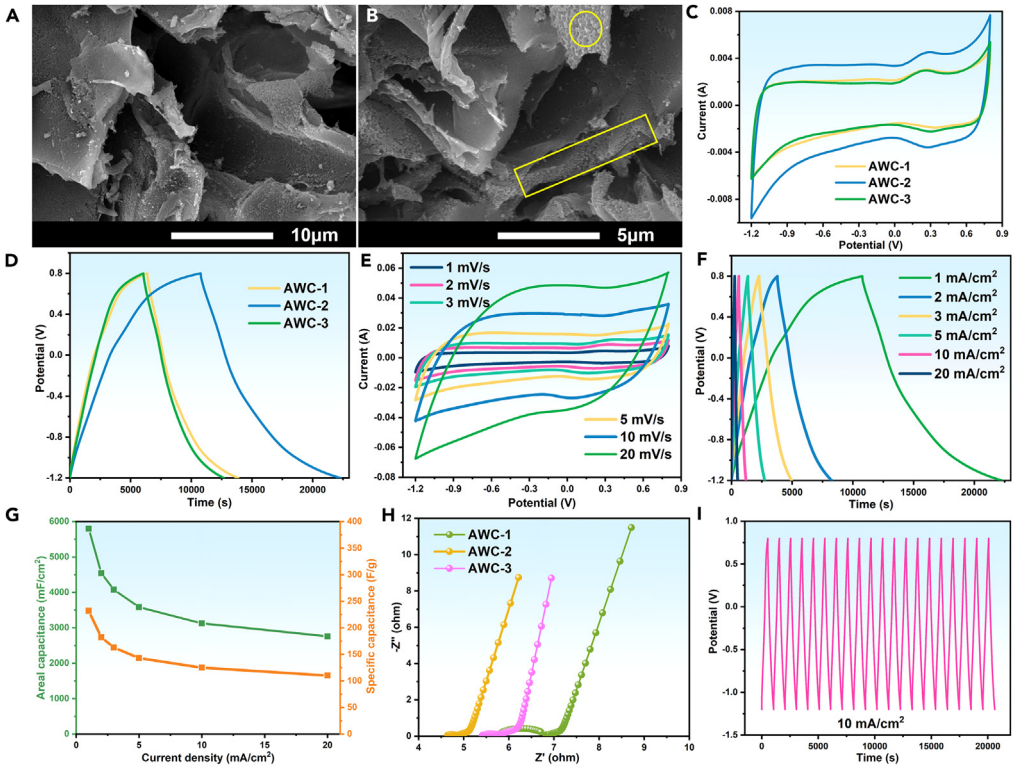

Figure 6. Microstructural and electrochemical characterizations of AWC electrodes

(A and B) SEM images of the AWC-2 electrode at different magnifications.

(C) CV curves of the AWC electrode at 1 mV s^{-1}.

(D) GCD curves of the AWC electrode at 1 mA cm^{-2}.

(E–I) Electrochemical performance of AWC-2: (E) CV curves at different scan rates. (F) GCD curves at different current densities. (G) Rate performance. (H) Nyquist diagram of the AWC-1, AWC-2, and AWC-3 electrodes. (I) Cycling performance of the AWC-2.

charging and discharging process, the contribution of pseudocapacitive behavior and diffusion control is quantitatively estimated. Specifically, the capacitive quantitative differentiation of the CV curve is performed according to Equation 4. Figure 7D shows the contribution of capacitance to the total storage charge (rose area) at 50 mV s^{-1} (see Figure S5 for other scan rates), with results demonstrating considerable capacitance contribution in the CV process of the ASC device. As the scan rate increases from 5 to 100 mV s^{-1}, the total proportion of the stored charge from the capacitive-controlled process gradually grows from 13% to 70% (Figure 7E), implying that capacitance plays a dominant role in the ASC storage electrochemical reaction. This is also one of the reasons for the excellent performance observed.

The calculation relations are as follows:

$$i = i_{cap} + i_{diff} = av^b, \quad \text{(Equation 2)}$$

$$\log i = \log a + b \log v, \quad \text{(Equation 3)}$$

where a and b are the adjustable parameters.

$$I(V) = k_1 v + k_2 v^{1/2}, \quad \text{(Equation 4)}$$

where i (V) is the current density response at a fixed potential, k_1 is the capacitive effect factor, k_2 is the diffusion process effect factor, and V is the scan rate. Thus, in Equation 4, $k_1 v$ and $k_2 v^{1/2}$ represent the pseudocapacitance contribution and diffusion-controlled contribution, respectively.

The GCD curves at different current densities are shown in Figure 7F. The approximately symmetrical triangular shape indicates ideal capacitance behavior for the ASC. The areal and specific capacitances of the ASC device were calculated according to the discharge curve (Figure 7G), with results showing areal and specific capacitances of 2.7, 2.4, 2.2, 1.7, and 1.3 F cm^{-2} and 96, 86, 79.4, 62, and 48 F g^{-1} at current densities of 1.0, 5.0, 10.0, 30.0, and 50 mA cm^{-2}, respectively. It is stimulating that the areal and specific capacitance of ASC can still reach 0.7 F cm^{-2} and 25 F g^{-1}, respectively, even at the high current density of 100 mA cm^{-2}. Energy and power density are also important parameters for the ASC. As seen in Figure 7H, the assembled ASC device displays extremely high energy densities (0.375–1.5 mWh cm^{-2} and

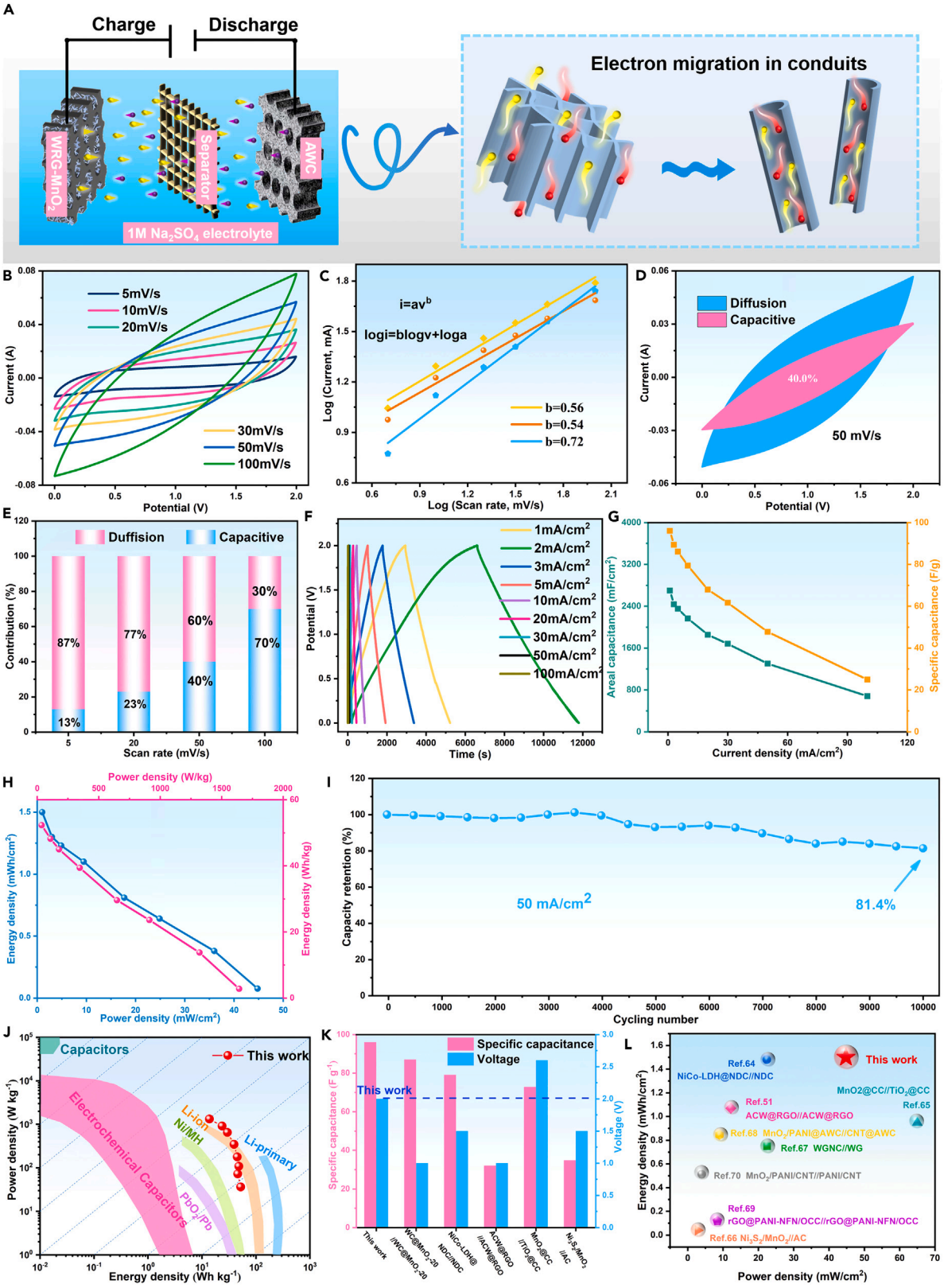
A
Charge
Discharge
WRG-MnO2
Separator
AWC
1M Na2SO4 electrolyte
Electron migration in conduits
B
5mV/s
10mV/s
20mV/s
30mV/s
50mV/s
100mV/s
Current (A)
Potential (V)
C
i=av^b
logi=blogv+loga
b=0.56
b=0.54
b=0.72
Log (Current, mA)
Log (Scan rate, mV/s)
D
Diffusion
Capacitive
40.0%
50 mV/s
Current (A)
Potential (V)
E
Duffision
Capacitive
87%
13%
77%
23%
60%
40%
30%
70%
Contribution (%)
Scan rate (mV/s)
F
1mA/cm2
2mA/cm2
3mA/cm2
5mA/cm2
10mA/cm2
20mA/cm2
30mA/cm2
50mA/cm2
100mA/cm2
Potential (V)
Time (s)
G
Areal capacitance (mF/cm2)
Specific capacitance (F/g)
Current density (mA/cm2)
H
Power density (W/kg)
Energy density (mWh/cm2)
Energy density (Wh/kg)
Power density (mW/cm2)
I
50 mA/cm2
81.4%
Capacity retention (%)
Cycling number
J
Capacitors
This work
Electrochemical Capacitors
Li-ion
Ni/MH
Li-primary
PbO2/Pb
Power density (W kg-1)
Energy density (Wh kg-1)
K
Specific capacitance
Voltage
This work
Specific capacitance (F g-1)
Voltage (V)
This work
NiCo-LDH@NDC//NDC
ACW@RGO//ACW@RGO
MnO2@CC//TiO2@CC
Ni3S2/MnO2//AC
L
This work
Ref.64 NiCo-LDH@NDC//NDC
Ref.51 ACW@RGO//ACW@RGO
Ref.65
Ref.68 MnO2/PANI@AWC//CNT@AWC
Ref.67 WGNC//WG
Ref.70 MnO2/PANI/CNT//PANI/CNT
Ref.69 rGO@PANI-NFN/OCC//rGO@PANI-NFN/OCC
Ref.66 Ni3S2/MnO2//AC
Energy density (mWh/cm2)
Power density (mW/cm2)

Figure 7. Electrochemical behavior of WRG-$_{20}$MnO$_2$//AWC-2 devices

(A) Model diagram of the WRG-$_{20}$MnO$_2$//AWC-2 ASC and schematic diagram of the electron migration path.
(B) CV curves at various scan rates from 5 to 100 mV s^{-1} in a potential window of 0–2 V.
(C) Log *i* vs. log *v* plots under different voltages.
(D) Capacitive contribution to total current at 50 mV s^{-1}.
(E) Contribution proportion of the capacitive- and diffusion-controlled process at different scan rates.
(F) GCD curves at different current densities from 1 to 100 mA cm^{-2} in a potential window of 0–2 V.
(G) Rate performances.
(H) Areal and specific energy/power density.
(I) Cycling performance at 50 mA cm^{-2} after 10,000 cycles.
(J) Ragone plots of the ASC device compared with other energy storage technologies.
(K) Comparison of the specific capacitance and voltage window of ASC with other devices.
(L) Comparison of the energy/power density of ASC with previously reported devices.

13.75–39.4 Wh kg^{-1}) and power densities (9.45–36 mW cm^{-2} and 346.5–1320 W kg^{-1}). Finally, the cyclic stability of the ASC devices was also evaluated (Figure 7I), with results showing that 81.4% of the initial capacitance of the WRG-$_{20}$MnO$_2$//AWC-2 was retained after 10,000 cycles at a current density of 50 mA cm^{-2}.

Figure 7J shows a Ragone diagram comparing different electrochemical energy storage technologies. The figure indicates that the WRG-$_{20}$MnO$_2$//AWC-2 ASC exhibit better energy and power density as compared to energy storage devices such as electrochemical capacitors, lead batteries (PbO$_2$/Pb), nickel–hydrogen batteries (Ni/MH), primary lithium batteries, and secondary lithium batteries (Li-primary and Li-ion batteries), effectively filling the gap between traditional capacitors and lithium-ion batteries. To more specifically demonstrate the obvious advantages of the ASC prepared in this study, the performance of the obtained device was compared with other devices reported in the literature. As shown in Figure 7K, the ASC exhibits excellent specific capacitance (96 F g^{-1}) and wide voltage window (0–2.0V), which is superior to many of the previously reported SC devices, including WC@MnO$_2$-20//WC@MnO$_2$-20 (87 F g^{-1}, 0–1 V),[63] NiCo-LDH@NDC//NDC (79.1 F g^{-1}, 0–1.5 V),[64] ACW@RGO//ACW@RGO (32.1 F g^{-1}, 0–1 V),[51] MnO$_2$@CC//TiO$_2$@CC (72.8 F g^{-1}, 0–2.6 V),[65] and Ni$_3$S$_2$/MnO$_2$//AC (34.8 F g^{-1}, 0–1.5 V).[66] In addition, we compared the energy density and power density of the ASC with other devices. As shown in Figure 7L, compared to NiCo-LDH@NDC//NDC (1.48 mWh cm^{-2}, 22.4 mW cm^{-2}),[64] ACW@RGO//ACW@RGO (1.07 mWh cm^{-2}, 12.2 mW cm^{-2}),[51] MnO$_2$@CC//TiO$_2$@CC (0.95 mWh cm^{-2}, 65.0 mW cm^{-2}),[65] Ni$_3$S$_2$/MnO$_2$//AC (0.04 mWh cm^{-2}, 2.88 mW cm^{-2}),[66] WGNC//WG (0.75 mWh cm^{-2}, 22.5 mW cm^{-2}),[67] MnO$_2$/PANI@AWC//CNT@AWC (0.85 mWh cm^{-2}, 9.0 mW cm^{-2}),[68] rGO@PANI-NFN/OCC//rGO@PANI-NFN/OCC (0.1179 mWh cm^{-2}, 8.42 mW cm^{-2}),[69] and MnO$_2$/PANI/CNT//PANI/CNT(0.5133 mWh cm^{-2}, 3.98 mW cm^{-2}),[70] the energy and power density (1.5 mWh cm^{-2} and 44.8 mW cm^{-2}, respectively) of the ASC presents a prominent performance advantage. This superiority may be due to the excellent performance of the layered RGO and icicle-shaped MnO$_2$ in the electrodes during the operation of the WRG-$_{20}$MnO$_2$//AWC-2 ASC. Our research results thus suggest broad application prospects for WRG-$_{20}$MnO$_2$//AWC-2 in the future.

DISCUSSION

In summary, hydrothermal regulation was used for the successful synthesis of a green WRG-$_{20}$MnO$_2$ electrode material without the need for adhesives. WC preserves the porous structure of natural wood, providing a fast pathway for electrons migration and ions diffusion. The high capacitance of the WRG-$_{20}$MnO$_2$ electrode (214 F g^{-1}/8.2 F cm^{-2} at 1 mA cm^{-2}) was achieved through the synergistic action of wood, graphene, and MnO$_2$. An ASC device (WRG-$_{20}$MnO$_2$//AWC-2) was constructed using WRG-$_{20}$MnO$_2$ as the cathode and AWC as the anode. Notably, the ASC device exhibits a wide voltage window (0–2 V), providing it with excellent energy density (0.375–1.5 mWh cm^{-2} and 13.75–52.3 Wh kg^{-1}) and power density (9.45–44.8 mW cm^{-2} and 346.5–1642.7 W kg^{-1}) as well as a long cycling life (with 81.4% of the capacitance retained over 10,000 cycles at 50 mA cm^{-2}). These exciting research results are attributed to the porous channels of wood, the excellent conductivity and high specific surface area of graphene, and the unique icicle-shaped nano MnO$_2$ structure. This study provides a new concept for the development and utilization of high-energy-density SCs while providing support for the application of biomass-based materials in the field of renewable electrochemical energy storage.

Limitations of the study

In this work, the 3D porous structure of wood has made a significant contribution to the excellent electrochemical performance of WRG-MnO2. However, wood is an anisotropic biomass material, and the stability of its performance still poses significant challenges in the research of wood-based energy storage materials. In addition, the structural design and load control of electrode materials will also be the focus of research in the following work, which is crucial for improving electrochemical performance.

STAR★METHODS

Detailed methods are provided in the online version of this paper and include the following:

- KEY RESOURCES TABLE
- RESOURCE AVAILABILITY
  - Lead contact

SUPPLEMENTAL INFORMATION

Supplemental information can be found online at https://doi.org/10.1016/j.isci.2024.109228.

ACKNOWLEDGMENTS

The authors gratefully acknowledge financial support from the Inner Mongolia Natural Science Foundation Project (2022MS03001, 2019BS03020), the Inner Mongolia Autonomous Region Science and Technology Plan Project(2022YFHH0134), the Sand Shrubs Fibrosis Energy Innovation Team Project (BR-12-01), and the Basic scientific research business fee project for universities directly under the Inner Mongolia Autonomous Region(BR22-12-01).

AUTHOR CONTRIBUTIONS

Conceptualization, Methodology, Formal analysis, Investigation, Writing – original draft, Writing – review and editing, X.F.S.; Writing – review and editing, L.W.; Resources, L.L.L, Y.Z., Z.H.F., and J.W.; Writing – review & editing, Supervision, Z.W., X.T.Z., and X.M.W.

DECLARATION OF INTERESTS

The authors declare no competing interests.

Received: November 22, 2023
Revised: January 13, 2024
Accepted: February 8, 2024
Published: February 16, 2024

REFERENCES

1. Luo, M., Yang, K., Zhang, D., Liu, C., Yang, P., Chen, W., and Zhou, X. (2021). Lignocellulose-based free-standing hybrid electrode with natural vessels-retained, hierarchically pores-constructed and active materials-loaded for high-performance hybrid oxide supercapacitor. Int. J. Biol. Macromol. *187*, 903–910. https://doi.org/10.1016/j.ijbiomac.2021.07.178.
2. Zhou, Y., Qi, H., Yang, J., Bo, Z., Huang, F., Islam, M.S., Lu, X., Dai, L., Amal, R., Wang, C.H., and Han, Z. (2021). Two-birds-one-stone: multifunctional supercapacitors beyond traditional energy storage. Energy Environ. Sci. *14*, 1854–1896. https://doi.org/10.1039/d0ee03167d.
3. Li, K., Teng, H., Sun, Q., Li, Y., Wu, X., Dai, X., Wang, Y., Wang, S., Zhang, Y., Yao, K., et al. (2022). Engineering active sites on nitrogen-doped carbon nanotubes/cobaltosic oxide heterostructure embedded in biotemplate for high-performance supercapacitors. J. Energy Storage *53*, 105094. https://doi.org/10.1016/j.est.2022.105094.
4. Dubal, D.P., Chodankar, N.R., Kim, D.H., and Gomez-Romero, P. (2018). Towards flexible solid-state supercapacitors for smart and wearable electronics. Chem. Soc. Rev. *47*, 2065–2129. https://doi.org/10.1039/c7cs00505a.
5. Li, K., Guo, Z., Sun, Q., Dai, X., Li, Y., Yao, K., Liu, X., Bao, Z., Rao, J., and Zhang, Y. (2023). Phosphorus vacancy regulation and interfacial coupling of biotemplate derived CoP@FeP2 heterostructure to boost pseudocapacitive reaction kinetics. Chem. Eng. J. *454*, 140223. https://doi.org/10.1016/j.cej.2022.140223.
6. Pan, Z., Yang, J., Zhang, Q., Liu, M., Hu, Y., Kou, Z., Liu, N., Yang, X., Ding, X., Chen, H., et al. (2019). All-Solid-State Fiber Supercapacitors with Ultrahigh Volumetric Energy Density and Outstanding Flexibility. Adv. Energy Mater. *9*, 1802753. https://doi.org/10.1002/aenm.201802753.
7. Wu, Z., Wang, Y., Liu, X., Lv, C., Li, Y., Wei, D., and Liu, Z. (2019). Carbon-Nanomaterial-Based Flexible Batteries for Wearable Electronics. Adv. Mater. *31*, e1800716. https://doi.org/10.1002/adma.201800716.
8. Han, Y., Lu, Y., Shen, S., Zhong, Y., Liu, S., Xia, X., Tong, Y., and Lu, X. (2019). Enhancing the Capacitive Storage Performance of Carbon Fiber Textile by Surface and Structural Modulation for Advanced Flexible Asymmetric Supercapacitors. Adv. Funct. Mater. *29*, 1806329. https://doi.org/10.1002/adfm.201806329.
9. Zhang, Q., Li, C., Li, Q., Pan, Z., Sun, J., Zhou, Z., He, B., Man, P., Xie, L., Kang, L., et al. (2019). Flexible and High-Voltage Coaxial-Fiber Aqueous Rechargeable Zinc-Ion Battery. Nano Lett. *19*, 4035–4042. https://doi.org/10.1021/acs.nanolett.9b01403.
10. Poonam, Sharma, K., Arora, A., and Tripathi, S.K. (2019). Review of supercapacitors: Materials and devices. J. Energy Storage *21*, 801–825. https://doi.org/10.1016/j.est.2019.01.010.
11. Xiong, C., Lin, X., Liu, H., Li, M., Li, B., Jiao, S., Zhao, W., Duan, C., Dai, L., and Ni, Y. (2019). Fabrication of 3D Expanded Graphite-Based (MnO2 Nanowalls and PANI Nanofibers) Hybrid as Bifunctional Material for High-Performance Supercapacitor and Sensor. J. Electrochem. Soc. *166*, A3965–A3971. https://doi.org/10.1149/2.0181916jes.
12. Zhang, X., Lin, Q., Zhang, X., and Peng, K. (2018). A novel 3D conductive network-based polyaniline/graphitic mesoporous carbon composite electrode with excellent electrochemical performance. J. Power Sources *401*, 278–286. https://doi.org/10.1016/j.jpowsour.2018.08.091.
13. Shwetha, K.P., Manjunatha, C., Sudha Kamath, M.K., Vinaykumar, Radhika, M.G.R., and Khosla, A. (2022). Morphology-controlled synthesis and structural features of ultrafine nanoparticles of Co3O4: An active electrode material for a supercapacitor. Appl. Res. *1*. https://doi.org/10.1002/appl.202200031.

14. Xiang, C., Wang, Q., Zou, Y., Huang, P., Chu, H., Qiu, S., Xu, F., and Sun, L. (2017). Simple synthesis of graphene-doped flower-like cobalt–nickel–tungsten–boron oxides with self-oxidation for high-performance supercapacitors. J. Mater. Chem. A Mater. *5*, 9907–9916. https://doi.org/10.1039/c7ta00234c.
15. Mohd Abdah, M.A.A., Azman, N.H.N., Kulandaivalu, S., and Sulaiman, Y. (2020). Review of the use of transition-metal-oxide and conducting polymer-based fibres for high-performance supercapacitors. Mater. Des. *186*, 108199. https://doi.org/10.1016/j.matdes.2019.108199.
16. Xiong, C., Li, B., Lin, X., Liu, H., Xu, Y., Mao, J., Duan, C., Li, T., and Ni, Y. (2019). The recent progress on three-dimensional porous graphene-based hybrid structure for supercapacitor. Compos. B Eng. *165*, 10–46. https://doi.org/10.1016/j.compositesb.2018.11.085.
17. Xiong, C., Li, T., Zhu, Y., Zhao, T., Dang, A., Li, H., Ji, X., Shang, Y., and Khan, M. (2017). Two-step approach of fabrication of interconnected nanoporous 3D reduced graphene oxide-carbon nanotube-polyaniline hybrid as a binder-free supercapacitor electrode. J. Alloys Compd. *695*, 1248–1259. https://doi.org/10.1016/j.jallcom.2016.10.253.
18. Chu, H., Fu, C., Xu, J., Li, W., Qian, J., Nie, W., and Ran, X. (2020). Carbon-doped inorganic nanoassemblies as fillers to tailor the dielectric and energy storage properties in polymer-based nanocomposites. Mater. Des. *188*, 108486. https://doi.org/10.1016/j.matdes.2020.108486.
19. Thangavel, R., Kannan, A.G., Ponraj, R., Thangavel, V., Kim, D.-W., and Lee, Y.-S. (2018). High-energy green supercapacitor driven by ionic liquid electrolytes as an ultra-high stable next-generation energy storage device. J. Power Sources *383*, 102–109. https://doi.org/10.1016/j.jpowsour.2018.02.037.
20. Chen, C., Zhang, Y., Li, Y., Dai, J., Song, J., Yao, Y., Gong, Y., Kierzewski, I., Xie, J., and Hu, L. (2017). All-wood, low tortuosity, aqueous, biodegradable supercapacitors with ultra-high capacitance. Energy Environ. Sci. *10*, 538–545. https://doi.org/10.1039/c6ee03716j.
21. Fu, Q., Ansari, F., Zhou, Q., and Berglund, L.A. (2018). Wood Nanotechnology for Strong, Mesoporous, and Hydrophobic Biocomposites for Selective Separation of Oil/Water Mixtures. ACS Nano *12*, 2222–2230. https://doi.org/10.1021/acsnano.8b00005.
22. Jiang, F., Li, T., Li, Y., Zhang, Y., Gong, A., Dai, J., Hitz, E., Luo, W., and Hu, L. (2018). Wood-Based Nanotechnologies toward Sustainability. Adv. Mater. *30*. https://doi.org/10.1002/adma.201703453.
23. Maziarka, P., Sommersacher, P., Wang, X., Kienzl, N., Retschitzegger, S., Prins, W., Hedin, N., and Ronsse, F. (2021). Tailoring of the pore structures of wood pyrolysis chars for potential use in energy storage applications. Appl. Energy *286*, 116431. https://doi.org/10.1016/j.apenergy.2020.116431.
24. Barthelat, F., Yin, Z., and Buehler, M.J. (2016). Structure and mechanics of interfaces in biological materials. Nat. Rev. Mater. *1*, 16007. https://doi.org/10.1038/natrevmats.2016.7.
25. Mao, B.S., Wen, Z., Bo, Z., Chang, J., Huang, X., and Chen, J. (2014). Hierarchical nanohybrids with porous CNT-networks decorated crumpled graphene balls for supercapacitors. ACS Appl. Mater. Interfaces *6*, 9881–9889. https://doi.org/10.1021/am502604u.
26. Cao, X., Zheng, B., Rui, X., Shi, W., Yan, Q., and Zhang, H. (2014). Metal oxide-coated three-dimensional graphene prepared by the use of metal-organic frameworks as precursors. Angew. Chem. Int. Ed. Engl. *53*, 1404–1409. https://doi.org/10.1002/anie.201308013.
27. Ahn, H.J., Kim, I.H., Yoon, J.C., Kim, S.I., and Jang, J.H. (2014). p-Doped three-dimensional graphene nano-networks superior to platinum as a counter electrode for dye-sensitized solar cells. Chem. Commun. *50*, 2412–2415. https://doi.org/10.1039/c3cc48920e.
28. Maiyalagan, T., Dong, X., Chen, P., and Wang, X. (2012). Electrodeposited Pt on three-dimensional interconnected graphene as a free-standing electrode for fuel cell application. J. Mater. Chem. *22*, 5286. https://doi.org/10.1039/c2jm16541d.
29. Sun, H., Mei, L., Liang, J., Zhao, Z., Lee, C., Fei, H., Ding, M., Lau, J., Li, M., Wang, C., et al. (2017). Three-dimensional holey-graphene/niobia composite architectures for ultrahigh-rate energy storage. Science *356*, 599–604.
30. Xiong, C., Li, B., Dang, W., Zhao, W., Duan, C., Dai, L., and Ni, Y. (2020). Co/CoS nanofibers with flower-like structure immobilized in carbonated porous wood as bifunctional material for high-performance supercapacitors and catalysts. Mater. Des. *195*, 108942. https://doi.org/10.1016/j.matdes.2020.108942.
31. Wang, Y., Lin, X., Liu, T., Chen, H., Chen, S., Jiang, Z., Liu, J., Huang, J., and Liu, M. (2018). Wood-Derived Hierarchically Porous Electrodes for High-Performance All-Solid-State Supercapacitors. Adv. Funct. Mater. *28*. https://doi.org/10.1002/adfm.201806207.
32. Wan, C., Jiao, Y., and Li, J. (2016). Core–shell composite of wood-derived biochar supported MnO2nanosheets for supercapacitor applications. RSC Adv. *6*, 64811–64817. https://doi.org/10.1039/c6ra12043a.
33. Teng, S., Siegel, G., Prestgard, M.C., Wang, W., and Tiwari, A. (2015). Synthesis and characterization of copper-infiltrated carbonized wood monoliths for supercapacitor electrodes. Electrochim. Acta *161*, 343–350. https://doi.org/10.1016/j.electacta.2015.02.117.
34. Shan, X., Wu, J., Zhang, X., Wang, L., Yang, J., Chen, Z., Yu, J., and Wang, X. (2021). Wood for Application in Electrochemical Energy Storage Devices. Cell Rep. Phys. Sci. *2*, 100654. https://doi.org/10.1016/j.xcrp.2021.100654.
35. Yan, J., Fan, Z., Wei, T., Qian, W., Zhang, M., and Wei, F. (2010). Fast and reversible surface redox reaction of graphene–MnO2 composites as supercapacitor electrodes. Carbon *48*, 3825–3833. https://doi.org/10.1016/j.carbon.2010.06.047.
36. Lee, S.W., Kim, J., Chen, S., Hammond, P.T., and Shao-Horn, Y. (2010). Carbon nanotube/manganese oxide ultrathin film electrodes for electrochemical capacitors. ACS Nano *4*, 3889–3896.
37. Chen, S., Zhu, J., Wu, X., Han, Q., and Wang, X. (2010). Graphene oxide– MnO2 nanocomposites for supercapacitors. ACS Nano *4*, 2822–2830.
38. He, S., Zhang, R., Zhang, C., Liu, M., Gao, X., Ju, J., Li, L., and Chen, W. (2015). Al/C/MnO2 sandwich nanowalls with highly porous surface for electrochemical energy storage. J. Power Sources *299*, 408–416. https://doi.org/10.1016/j.jpowsour.2015.09.029.
39. Guo, J., Yu, Y., Sun, L., Zhang, Z., Zhao, Y., Chai, R., and Shi, K. (2020). Bio-inspired multicomponent carbon nanotube microfibers from microfluidics for supercapacitor. Chem. Eng. J. *397*, 125517. https://doi.org/10.1016/j.cej.2020.125517.
40. Song, L., Cao, X., Li, L., Wang, Q., Ye, H., Gu, L., Mao, C., Song, J., Zhang, S., and Niu, H. (2017). General Method for Large-Area Films of Carbon Nanomaterials and Application of a Self-Assembled Carbon Nanotube Film as a High-Performance Electrode Material for an All-Solid-State Supercapacitor. Adv. Funct. Mater. *27*. https://doi.org/10.1002/adfm.201700474.
41. Huang, R., Huang, M., Li, X., An, F., Koratkar, N., and Yu, Z.Z. (2018). Porous Graphene Films with Unprecedented Elastomeric Scaffold-Like Folding Behavior for Foldable Energy Storage Devices. Adv. Mater. *30*, e1707025. https://doi.org/10.1002/adma.201707025.
42. Xu, T., Yang, D., Zhang, S., Zhao, T., Zhang, M., and Yu, Z.-Z. (2021). Antifreezing and stretchable all-gel-state supercapacitor with enhanced capacitances established by graphene/PEDOT-polyvinyl alcohol hydrogel fibers with dual networks. Carbon *171*, 201–210. https://doi.org/10.1016/j.carbon.2020.08.071.
43. Xu, T., Yang, D., Fan, Z., Li, X., Liu, Y., Guo, C., Zhang, M., and Yu, Z.-Z. (2019). Reduced graphene oxide/carbon nanotube hybrid fibers with narrowly distributed mesopores for flexible supercapacitors with high volumetric capacitances and satisfactory durability. Carbon *152*, 134–143. https://doi.org/10.1016/j.carbon.2019.06.005.
44. Yang, Y., Ng, S.W., Chen, D., Chang, J., Wang, D., Shang, J., Huang, Q., Deng, Y., and Zheng, Z. (2019). Freestanding Lamellar Porous Carbon Stacks for Low-Temperature-Foldable Supercapacitors. Small *15*, e1902071. https://doi.org/10.1002/smll.201902071.
45. Wang, Y., Liu, R., Tian, Y., Sun, Z., Huang, Z., Wu, X., and Li, B. (2020). Heteroatoms-doped hierarchical porous carbon derived from chitin for flexible all-solid-state symmetric supercapacitors. Chem. Eng. J. *384*, 123263. https://doi.org/10.1016/j.cej.2019.123263.
46. Yin, J., Zhang, W., Alhebshi, N.A., Salah, N., and Alshareef, H.N. (2020). Synthesis Strategies of Porous Carbon for Supercapacitor Applications. Small Methods *4*. https://doi.org/10.1002/smtd.201900853.
47. Zhang, Z., Lee, C.-S., and Zhang, W. (2017). Vertically Aligned Graphene Nanosheet Arrays: Synthesis, Properties and Applications in Electrochemical Energy Conversion and Storage. Adv. Energy Mater. *7*. https://doi.org/10.1002/aenm.201700678.
48. Pan, B., Bai, L., Hu, C.M., Wang, X., Li, W.S., and Zhao, F.G. (2020). Graphene-Indanthrone Donor–π–Acceptor Heterojunctions for High-Performance Flexible Supercapacitors. Adv. Energy Mater. *10*. https://doi.org/10.1002/aenm.202000181.
49. Khazaeli, A., Godbille-Cardona, G., and Barz, D.P.J. (2020). A Novel Flexible Hybrid

Battery–Supercapacitor Based on a Self-Assembled Vanadium-Graphene Hydrogel. Adv. Funct. Mater. *30*. https://doi.org/10.1002/adfm.201910738.

50. Zhao, S., Fang, R., Sun, Z., Wang, S., Veder, J.P., Saunders, M., Cheng, H.M., Liu, C., Jiang, S.P., and Li, F. (2018). A 3D Multifunctional Architecture for Lithium–Sulfur Batteries with High Areal Capacity. Small Methods *2*. https://doi.org/10.1002/smtd.201800067.
51. Wu, J., Dai, Q., Li, X., Li, W., Hao, S.M., Zeng, M.J., and Yu, Z.Z. (2021). Wood-Derived Monolithic Ultrathick Porous Carbon Electrodes Filled with Reduced Graphene Oxide for High-Performance Supercapacitors with Ultrahigh Areal Capacitances. Chemelectrochem *8*, 4328–4336. https://doi.org/10.1002/celc.202100937.
52. Zhu, L., Wang, J., Rong, S., Wang, H., and Zhang, P. (2017). Cerium modified birnessite-type MnO2 for gaseous formaldehyde oxidation at low temperature. Appl. Catal. B Environ. *211*, 212–221. https://doi.org/10.1016/j.apcatb.2017.04.025.
53. Yang, W., Zhu, Y., You, F., Yan, L., Ma, Y., Lu, C., Gao, P., Hao, Q., and Li, W. (2018). Insights into the surface-defect dependence of molecular oxygen activation over birnessite-type MnO2. Appl. Catal. B Environ. *233*, 184–193. https://doi.org/10.1016/j.apcatb.2018.03.107.
54. Li, Y., Fu, K.K., Chen, C., Luo, W., Gao, T., Xu, S., Dai, J., Pastel, G., Wang, Y., Liu, B., et al. (2017). Enabling high-areal-capacity lithium–sulfur batteries: designing anisotropic and low-tortuosity porous architectures. ACS Nano *11*, 4801–4807.
55. Buciuman, F., Patcas, F., Craciun, R., and Zahn, D.R.T. (1999). Vibrational spectroscopy of bulk and supported manganese oxides. Phys. Chem. Chem. Phys. *1*, 185–190. https://doi.org/10.1039/a807821a.
56. Li, K., Liu, X., Zheng, T., Jiang, D., Zhou, Z., Liu, C., Zhang, X., Zhang, Y., and Losic, D. (2019). Tuning MnO2 to FeOOH replicas with bio-template 3D morphology as electrodes for high performance asymmetric supercapacitors. Chem. Eng. J. *370*, 136–147. https://doi.org/10.1016/j.cej.2019.03.190.
57. Nirmaladevi, S., and Palanisamy, P.N. (2021). Adsorptive behavior of biochar and zinc chloride activated hydrochar prepared from Acacia leucophloea wood sawdust: kinetic equilibrium and thermodynamic studies. Desalination Water Treat. *209*, 170–181. https://doi.org/10.5004/dwt.2021.26515.
58. BoopathiRaja, R., and Parthibavarman, M. (2020). The cost-effective asymmetric supercapacitor from binary MnCo2O4 electrodes with nanofiber and nanocube-like morphology. J. Mater. Sci. Mater. Electron. *31*, 10151–10160. https://doi.org/10.1007/s10854-020-03560-y.
59. Zu, L., Zhang, W., Qu, L., Liu, L., Li, W., Yu, A., and Zhao, D. (2020). Mesoporous Materials for Electrochemical Energy Storage and Conversion. Adv. Energy Mater. *10*. https://doi.org/10.1002/aenm.202002152.
60. Ren, Z., Li, Y., and Yu, J. (2018). A Flexible Supercapacitor with High True Performance. iScience *9*, 138–148. https://doi.org/10.1016/j.isci.2018.10.016.
61. Zhou, C., Zhang, Y., Li, Y., and Liu, J. (2013). Construction of high-capacitance 3D CoO@polypyrrole nanowire array electrode for aqueous asymmetric supercapacitor. Nano Lett. *13*, 2078–2085. https://doi.org/10.1021/nl400378j.
62. Liu, J., Wang, J., Xu, C., Jiang, H., Li, C., Zhang, L., Lin, J., and Shen, Z.X. (2018). Advanced Energy Storage Devices: Basic Principles, Analytical Methods, and Rational Materials Design. Adv. Sci. *5*, 1700322. https://doi.org/10.1002/advs.201700322.
63. Chen, L., Wang, F., Tian, Z., Guo, H., Cai, C., Wu, Q., Du, H., Liu, K., Hao, Z., He, S., et al. (2022). Wood-Derived High-Mass-Loading MnO(2) Composite Carbon Electrode Enabling High Energy Density and High-Rate Supercapacitor. Small *18*, e2201307. https://doi.org/10.1002/smll.202201307.
64. Li, Z., Wang, X., Wang, Z., Wang, L., Guo, Y., Zhou, C., Li, X., Du, K., and Luo, Y. (2022). Nickel-cobalt layered double hydroxide nanosheets anchored to the inner wall of wood carbon tracheids by nitrogen-doped atoms for high-performance supercapacitors. J. Colloid Interface Sci. *608*, 70–78. https://doi.org/10.1016/j.jcis.2021.09.127.
65. Gu, Y.J., Wen, W., and Wu, J.M. (2020). Wide potential window TiO2@carbon cloth and high capacitance MnO2@carbon cloth for the construction of a 2.6 V high-performance aqueous asymmetric supercapacitor. J. Power Sources *469*, 228425.
66. Thejas Prasannakumar, A., R, R., Cherusseri, J., RMohan, R., and J Varma, S. (2022). High areal capacitance and long cycling stability in asymmetric supercapacitors using binder-free, hierarchical nanostructured Ni3S2/MnO2 hybrid electrodes. J. Energy Storage *55*, 105723. https://doi.org/10.1016/j.est.2022.105723.
67. Liu, Z., Wu, H., Li, Y., Song, J., Zhang, W., Yuan, H., Imtiaz, M., Zhu, S., and Lian, K. (2020). Redox active coating on graphite surface of hierarchically porous wood electrodes for supercapacitor application. Mater. Today Commun. *24*, 101045. https://doi.org/10.1016/j.mtcomm.2020.101045.
68. Wang, L., Wang, X., Ouyang, J., Guo, Y., Xiong, W., Zhao, L., Li, M., Hua, Z., Li, Z., Du, K., et al. (2023). Construction of polyaniline/MnO2 core-shell nanocomposites in carbonized wood tracheids for high-performance all-solid-state asymmetric supercapacitors. Appl. Surf. Sci. *612*, 155821. https://doi.org/10.1016/j.apsusc.2022.155821.
69. Wang, S., Li, Y., Xu, Q., Fu, Q., Guo, X., Zheng, Y., Zhang, W., Cao, Z., Li, R., and Ren, J. (2022). Facile preparation of graphene@polyaniline nanofiber network/oxidized carbon cloth composites for high-performance flexible solid-state supercapacitors. Nanoscale *14*, 15908–15917. https://doi.org/10.1039/d2nr04723c.
70. Luo, Z., Kou, B., Wang, Y., Song, Y., Weng, M., Liu, C., Zhang, W., and Chen, L. (2022). Toy-blocks-inspired programmable supercapacitors with high energy density. Chem. Eng. J. *445*, 136788. https://doi.org/10.1016/j.cej.2022.136788.
71. Shan, X., Wang, L., Wu, J., and Wang, X. (2021). Preparation of Wood-based Graphene Material and Its Three-dimensional Electrical Conductivity. J. Northeast For. Univ. *50*, 123–130. https://doi.org/10.13759/j.cnki.dlxb.2022.01.019.

STAR★METHODS

KEY RESOURCES TABLE

REAGENT or RESOURCE	SOURCE	IDENTIFIER
Chemicals, peptides, and recombinant proteins		
Potassium permanganate	Fuchen (Tianjin) Chemical Reagent Co., Ltd	CAS : 7722-64-7
Sodium sulphate anhydrous	Fuchen (Tianjin) Chemical Reagent Co., Ltd	CAS: 7757.82-6
Ascorbic acid	China National Pharmaceutical Group Chemical Reagent Co., Ltd	CAS: 50-81-7
Anhydrous ethanol	Fuchen (Tianjin) Chemical Reagent Co., Ltd	CAS: 64-17-5
Graphene oxide	individual	N/A

RESOURCE AVAILABILITY

Lead contact

Further information and requests for resources and reagents should be directed to and will be fulfilled by the lead contact, Ximing Wang (wangximing@imau.edu.cn).

Materials availability

This study did not generate new unique reagents.

Data and code availability

- Data reported in this paper will be shared by the lead contact upon request.
- This paper does not report original code.
- Any additional information required to reanalyze the data reported in this paper is available from the lead contact upon request.

METHOD DETAILS

Materials

Eleven-year-old poplar was selected from a fast-growing plantation as the base material and straight-grained sapwood boards with a 151% initial moisture content were obtained from Hohhot, Inner Mongolia Autonomous Region, China. GO was prepared using the improved Hummers method.[71] All chemicals used in this work were newly purchased and used without further purification and were of analytical grade.

Synthesis of a WRG conductive precursor

Wood samples were immersed in a 4 g/L GO solution, and wood@GO composites were obtained by drying at 53°C for 24 h. The WRG conductive precursor was then constructed using a two-step reduction method. (1) chemical reduction: the WC@GO composites were immersed in an ascorbic acid solution (3 g/L) at 80°C for 3 h. (2) Physical thermal reduction: to further modify the structural integrity of GO, the obtained materials were placed into a tubular furnace in a protective N_2 atmosphere, heated at 5 °C min^{-1}, and stabilized at 260°C for over 2 h. Samples were then carbonized at 1000°C for 2 h before the temperature was decreased to 25 °C at a cooling rate of 10 °C min^{-1}.

Preparation of the WRG-MnO_2 cathode

The WRG-MnO_2 composite electrode was synthesized using a highly scalable hydrothermal method. First, a mixed solution of $KMnO_4$ and Na_2SO_4 (1:1) was prepared and stirred at room temperature until completely dissolved. The WRG precursor was then immersed in the solution before transferring to a 50-mL Teflon-lined autoclave, where it was reacted at 120°C for 3 h. Samples were then cooled to 25°C, washed multiple times with absolute ethanol and DI, and dried at 53°C for 24 h to obtain the WRG-MnO_2 electrode. To study how MnO_2 affects the electrochemical properties, electrodes with different $KMnO_4$ concentrations (5, 10, 20, and 30 mM) were prepared and denoted as WRG-$_5$$MnO_2$, WRG-$_{10}$$MnO_2$, WRG-$_{20}$$MnO_2$, and WRG-$_{30}$$MnO_2$, respectively.

Fabrication of the AWC anode

Preprepared thin wood slices were placed in a tube furnace in a N_2 atmosphere, precarbonized at 260°C for 2 h, and carbonized at 1000°C for 2 h before cooling to 25°C. The obtained WC was then placed in a tube furnace and physically activated in a CO_2 atmosphere at 800°C before cooling to 25°C to obtain the AWC electrode. Heating and cooling were performed at 5 °C min^{-1} and 10°C min^{-1}, respectively. The effect of

activation time on the electrochemical performance was also studied by subjecting the electrodes to different activation periods (1, 2, and 3 h), and the obtained samples were denoted as AWC-1, AWC-2, and AWC-3, respectively.

Materials characterization

The conductivity of WRG-MnO_2 was tested using a four-probe tester (RTS-8, Britain). The morphologies of the sections were observed via scanning electron microscopy (SEM, S-4800I, Japan) and transmission electron microscopy (TEM, FEI Tecnai G2, America). Material elements were analyzed via energy-dispersive X-ray spectrometry (Bruker QUANTAX 200, Germany). The structure of the material was characterized via X-ray diffraction (XRD, TD-3500, China). The chemical composition of the slices was analyzed via X-ray photoelectron spectroscopy (XPS, AXIS Ultra DLD, Japan). Raman spectra were recorded at 633 nm using a Raman spectrometer (Raman, Jobin Yvon HR-Evolution 2, France). The specific surface area was calculated using the Brunauer–Emmett–Teller (BET) method, and the pore size distribution and pore volume were calculated using the Barrett–Joyner–Halenda (BJH) method.

Electrochemical measurements

The electrochemical properties of the electrodes were evaluated in a 1.0-M Na_2SO_4 electrolyte using a three-electrode test cell with a Chi 660E electrochemical workstation (Shanghai Chenhua Instrument Co., Ltd.). A platinum electrode was used as the counter electrode, an Ag/AgCl electrode was used as the reference electrode, and the synthesized WRG-MnO_2 electrode without polymer binders was used as the working electrode. Cyclic voltammetry (CV) and galvanostatic charge–discharge (GCD) curves were obtained at a voltage window of 0–0.8 V. Electrochemical impedance spectroscopy was performed in the frequency range of 10^5–10^{-2} Hz. The areal (C_s, F cm^{-2}) and specific (C_m, F g^{-1}) capacitances were calculated based on the GCD curves using Equations 5 and 6.

$$C_s = \frac{I\Delta t}{s\Delta V}, \quad \text{(Equation 5)}$$

$$C_m = \frac{I\Delta t}{m\Delta V}, \quad \text{(Equation 6)}$$

where I (A) is the discharge current, Δt (s) is the discharge time, ΔV (V) is the potential window, s (cm^2) is the area of the electrode that was exposed to the electrolyte, and m (g) is the mass of the active materials in the electrode.

Asymmetric supercapacitors (ASCs) were assembled using the WRG-MnO_2 and AWC electrodes, i.e., WRG-$_{20}MnO_2$//AWC-2. The electrochemical performances of the SCs were evaluated in a two-electrode test system. The energy density (E, Wh kg^{-1}) and power density (P, W kg^{-1}) were calculated based on the GCD discharge curve using Equations 7 and 8.

$$E = \frac{1}{2}C\Delta V^2, \quad \text{(Equation 7)}$$

$$P = \frac{E}{\Delta t}, \quad \text{(Equation 8)}$$

where ΔV(V) is the voltage drop and Δt (s) is the discharging time.